Mechanical anisotropy of shape-memory NiTi with two-dimensional networks of micro-channels

Anselm J. Neurohr, David C. Dunand *

Department of Materials Science and Engineering, Northwestern University, Evanston, IL 60208, USA

Abstract

Ni–51.4 at.% Ti (Nitinol) containing 24 and 34 vol.% orthogonally interweaving micro-channels with 350–400 μm diameters was fabricated by a powder-metallurgy method. NiTi powder preforms containing steel wire meshes arranged in parallel layers were hot-pressed into NiTi/steel composites, from which the meshes were removed electrochemically, thereby producing micro-channels with tailorable morphology, fraction, and orientation. The compressive stiffness (15–35 GPa) and strength (420–780 MPa) can be controlled by the volume fraction and orientation of the micro-channels. Stiffness values are compared against analytical foam and composite models. A combination of elasticity, superelasticity, and the shape-memory effect allows for high strain recovery (93–95% of an applied compressive strain of 5%).

© 2011 Acta Materialia Inc. Published by Elsevier Ltd. All rights reserved.

Keywords: Porous material; Nickel titanium; Nitinol; Shape memory; Space-holder

1. Introduction

The unique shape-memory and superelastic properties of nickel–titanium (NiTi) alloys – combined with their high strength and ductility, large energy absorption and damping capacity, and good corrosion resistance and biocompatibility – render them useful for various multifunctional applications. NiTi foams combine these properties with those inherent to porous structures, such as low density and stiffness, high surface area, and high energy absorption by pore plastic collapse. Applications of NiTi foams include actuators [1], bone implants [2–5], energy absorbers and dampers [6–8], and for impedance matching between different materials [8].

Tailoring the pore shape and orientation can provide additional control over the physical properties of a foam. For instance, foams with aligned and elongated pores have a higher strength and stiffness in the direction of alignment than foams with a similar volume fraction of equiaxed pores [9–11], which is advantageous for sandwich cores. NiTi foams for orthopedic implant applications would also benefit from elongated pores that mimic the internal architecture of bone and provide improved bone and vasculature ingrowth for implant fixation [12,13]. Furthermore, micro-channels increase fluid permeability and are ubiquitous in micro-fluidics devices such as micro-pumps and actuators [14]. Another benefit of tailoring pore properties in NiTi is the prospect of fabricating porosity gradients. This is useful for impedance matching at connecting joints and interfaces [15].

Most previous investigations on NiTi have focused on the fabrication of porous structures with uniformly distributed equiaxed pores and isotropic mechanical properties by techniques such as partial sintering [16–25], hot isostatic pressing (HIP) followed by argon expansion [8,26–28], metal injection molding (MIM) followed by sintering [29] or self-propagating high-temperature synthesis (SHS) [30], transient liquid phase sintering by the addition of niobium [31,32], and powder consolidation in the presence of various space-holder materials [29,33–39]. Powder metallurgy is preferred over liquid processing routes because

---

* Corresponding author. Tel.: +1 847 491 5370.
  E-mail address: dunand@northwestern.edu (D.C. Dunand).

the Ni/Ti ratio is more easily controlled, which is critical for retaining the superelastic and shape-memory properties of NiTi [40]. Furthermore, NiTi has a high melting point (1310 °C), and its high titanium content makes it reactive with crucibles and residual gases, and susceptible to contamination in the liquid state.

Elongated pores have previously been created in NiTi by continuous zone melting with gas evolution [10,11] and SHS [41–43]. The former produces pores at the liquid/solid interface upon solidification of a NiTi melt into which hydrogen gas had been dissolved. The pores are cylindrical and aligned along the solidification direction, but control over pore shape and interconnectivity is limited. In SHS, reaction of a compact of mixed elemental nickel and titanium powders is initiated at one point to produce an exothermic reaction, which in turn propagates into adjacent layers of powders. A heat front traverses the powder compact and produces elongated pores parallel to the propagation direction. Since elemental powders are used, this process very often forms non-equiatomic intermetallic phases (e.g., Ti_2Ni, Ni_3Ti, and Ni_4Ti_3) that are no longer superelastic and cause embrittlement [16,44,45]. Laser engineered net shaping (LENS) was recently used to fabricate NiTi scaffolds with equiaxed pores with closely controlled morphology [46], as previously done with titanium [47]. However, a sizable fraction of the porosity stems from incomplete sintering of the powders, which reduces the strength and ductility of metallic foams and probably impairs fatigue resistance.

The space-holder method is best suited for independently controlling pore morphology, orientation, and volume fraction. In this method, elemental nickel and titanium or pre-alloyed NiTi powders are densified around temporary or permanent space-holders. When the space-holders are removed, pores are created that replicate their shape. Temporary (or "fugitive") space-holders are removed during the NiTi powder densification step by evaporation or thermal decomposition [29,33–36]. Permanent space-holders are removed after that step, thus avoiding pore collapse when high-pressure sintering is employed. This method is preferred when precise replication of the space-holder and full densification of the metallic scaffold are desired. In the past, sodium chloride [29,38,39] and sodium fluoride [37] were used as permanent space-holders in NiTi foams. They were removed by dissolution in water after densification of the NiTi matrix, resulting in foams with equiaxed pores replicating the shape of the initial space-holder powders.

In the following research, we use a procedure initially demonstrated for titanium [48] and for Ti–6Al–4V [49,50] and adapted to NiTi for the fabrication of networks of micro-channels [51]. Steel wire meshes were used as permanent space-holders and removed electrochemically after densification of NiTi powders by hot-pressing. The mechanical and shape memory properties of the porous NiTi are evaluated along various directions and the anisotropic stiffness behavior is compared to simple model predictions.

2. Experimental procedures

2.1. Composite densification

The processing steps are described in detail in Ref. [51] and are summarized hereafter for clarity. Pre-alloyed NiTi powder (Fig. 1a), with a nominal composition of 48.6 at.% Ni (99.9% purity, Special Metal Corp., NY), were sieved to a size range of 63–177 μm. Their smooth, spherical shape is typical of fabrication by liquid spraying. Two types of low-carbon steel wire meshes with an interweaving orthogonal pattern were used as space-holders (Fig. 1b and c): one with 356 μm diameter wires spaced 711 μm apart ("coarse mesh"); and the other with 406 μm diameter wires spaced 432 μm apart ("fine mesh"). The meshes were first carburized in packs containing pure carbon powder for 2 h at 960 °C in air. Previous testing showed that this procedure prevents interdiffusion between the steel and the NiTi through the formation of a TiC layer at the steel/NiTi interface [51].

Layers of NiTi powders were poured into a 25.4 mm diameter die, alternating with meshes that had been cut into 25.4 mm diameter disks. The contacting surfaces of the die and punches were lubricated with boron nitride. To ensure that the meshes were parallel, they were each manually compacted after being placed onto a layer of NiTi powder.

Two NiTi/steel composites were fabricated in this manner. Composite HP (for "high porosity") was created by alternating 19 layers of NiTi powders (1.74 g per layer) alternating with 18 meshes (fine mesh). To ensure that the final foams have an isotropic pore microstructure the meshes were rotated by 0°, −15°, +15°, −30°, +30°, −45°, −38°, +38°, −23°, +23°, −8°,+8°, 0°, −15°, +15°, −30°, +30°, and −45°, in the above order. Composite LP (for "low porosity") was made by alternating 18 layers of NiTi powders (2.1 g per layer) with 17 meshes (coarse mesh) following the same orientation pattern. The nominal open areas of the coarse and fine meshes were 44% and 27% respectively, resulting in different volume fractions of steel. A monolithic control sample was made by pouring NiTi powders without any mesh space-holders into the die.

The mesh/powder preforms were then hot-pressed under vacuum (<10^{-6} torr) at 1020 °C, below the Fe–Ni–Ti eutectic point (>1100 °C [52]) in an instrumented hot-press described in more details in Ref. [53]. Densification of specimen HP was achieved after hot-pressing for 3 h at a uniaxial pressure of 40 MPa followed by 3 h at 60 MPa. Specimen LP and the control sample were pressed for 3 h at 60 MPa. The punch displacement was measured to monitor the densification of the powders. After hot-pressing, the composites were cooled under vacuum for ∼3 h under low stress (∼0.5 MPa) to room temperature.

2.2. Space-holder removal

Twelve parallelepipeds (5 × 5 × 10 mm) were electric discharge machined from the densified NiTi/steel composites so
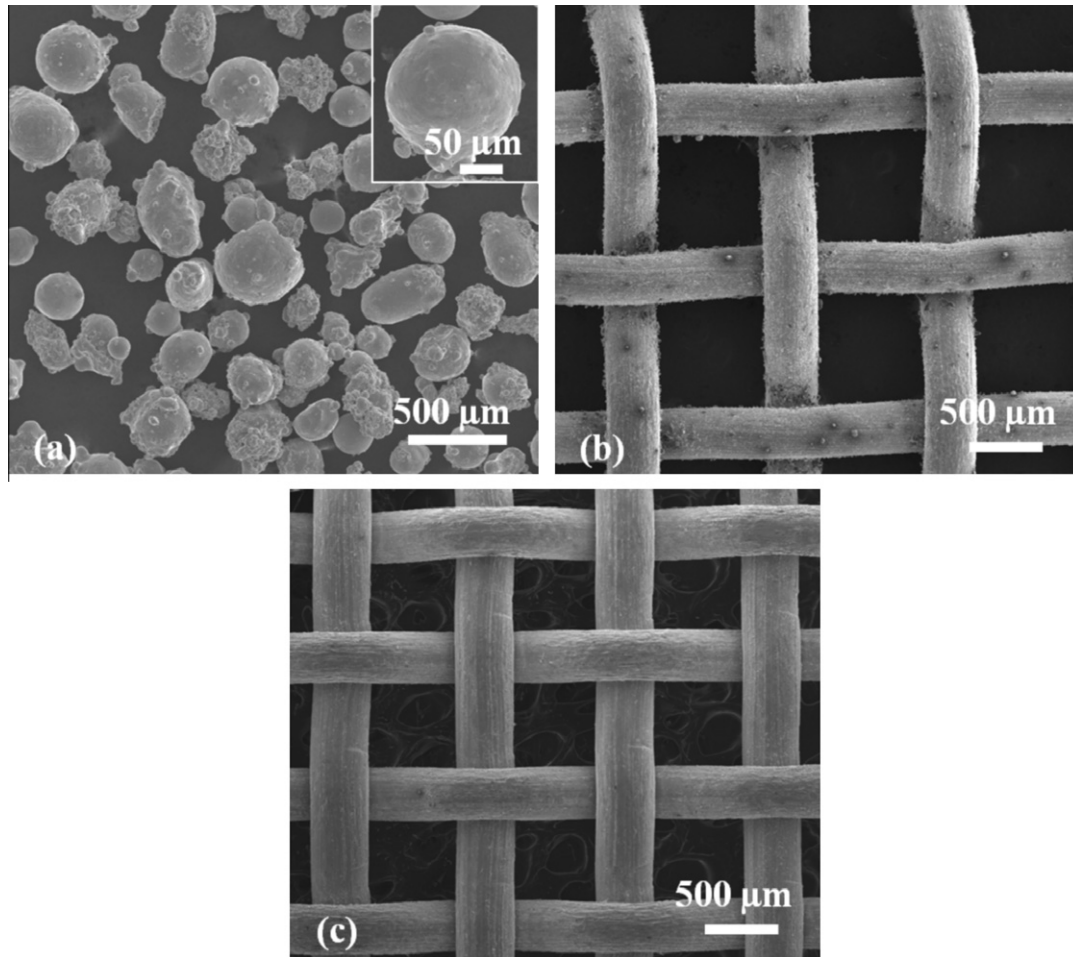
Fig. 1. Scanning electron micrographs of (a) the initial NiTi powders, (b) a coarse steel mesh, and (c) a fine steel mesh.

that the steel wires were exposed to the surface. They were cut at various orientations so that the angle between the mesh plane and the long direction of the specimen was 0°, 45°, or 90° for composite LP and 0° or 90° for composite HP.

The steel/NiTi composites were then attached to a commercially pure titanium (cp-Ti) anode with Nylon wire and immersed in electrolyte (saturated NaCl solution with 3% acetic acid) inside a glass beaker. A 500 μm thick cp-Ti cathode was wrapped around the inside wall of the beaker and a DC voltage of 0.8 V was supplied across the electrodes. The less noble steel corroded preferentially while the NiTi was protected by a passivating oxide layer, producing elongated and interweaving micro-channels in the densified NiTi matrix replicating the mesh wires. The beaker was placed into an ultrasonic bath to accelerate the removal of the steel by removing iron oxide and replenishing the electrolyte at the reaction surfaces. The mass of the specimen was measured periodically to track the dissolution progress. Comparing the mass lost to the original mass fraction of steel revealed when the dissolution of the meshes was complete, which was also indicated by the onset of discoloration on the NiTi surface. Dissolution times ranged from 25 h to 62 h, depending on the type of steel mesh space-holder used.

Hereafter, the specimens are referred to by their porosity followed by the orientation of their porous layers with respect to the long dimension of the specimen (i.e., the loading direction). For instance, LP90 refers to a low porosity sample where the planes of the porous layers are perpendicular to the loading direction. Such a foam is shown in Fig. 2a, and the arrows in Fig. 2a–e indicate the direction of the compression tests for the five types of samples studied.

2.3. Microstructural characterization

The microstructure was studied by scanning electron (SEM) and optical microscopy (OM). Samples were first ground to 320 μm grit size and polished with diamond and alumina suspensions to 9 μm, 3 μm, and finally 0.5 μm grit. Mass and volume measurements of the specimens were used to calculate the total porosity and helium pycnometry provided the closed porosity (using 6.45 g cm^{-3} as the density of bulk NiTi [54]). The open porosity was taken as the difference between total and closed porosity.

Differential scanning calorimetry (DSC) was used to measure the phase transformation behavior. The tests were conducted on ~20 mg samples under nitrogen cover gas
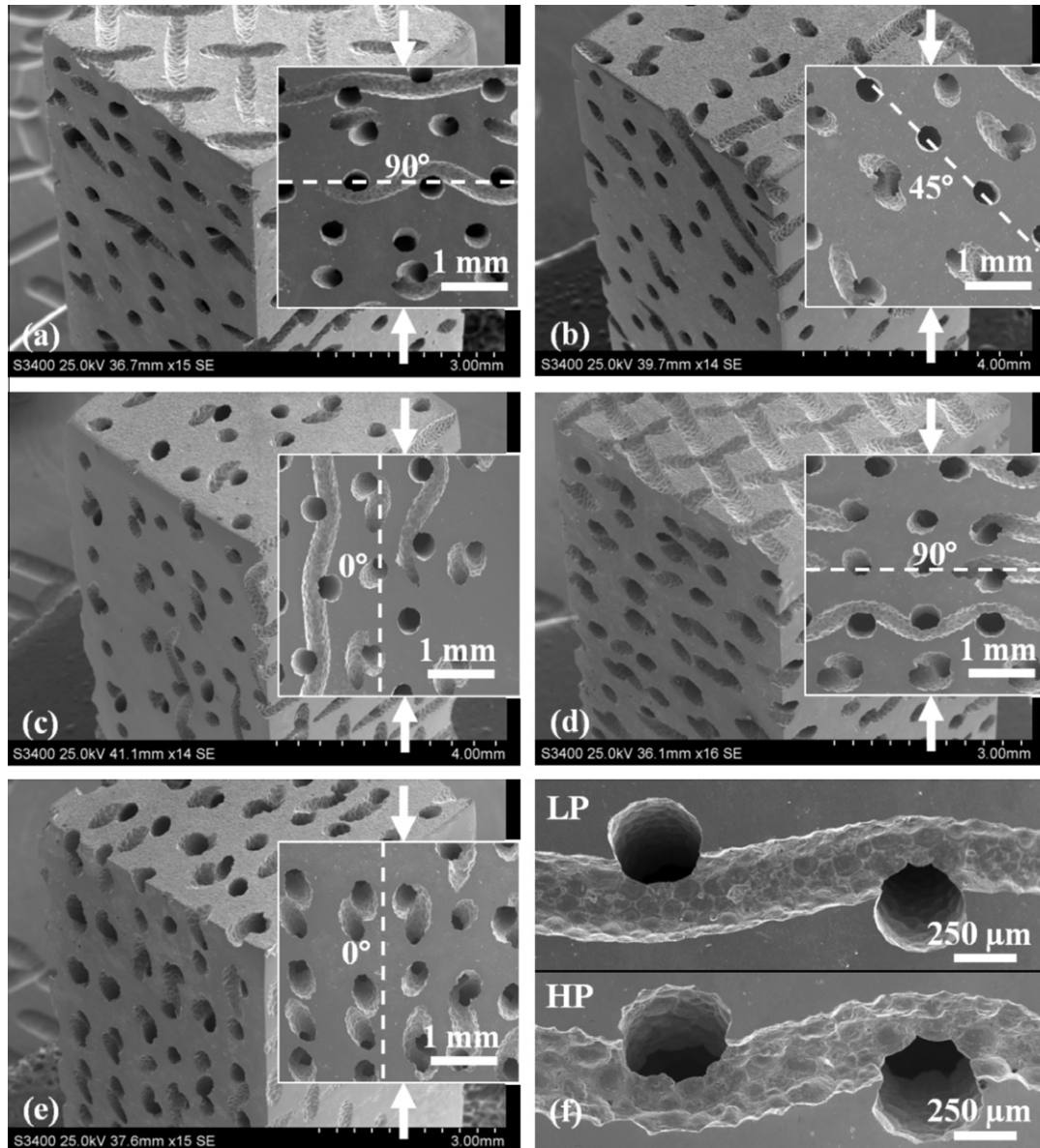
Fig. 2. Scanning electron micrographs of samples (a) LP90 [51], (b) LP45, (c) LP0, (d) HP90 [51], and (e) HP0. The inset images show the channel orientation (indicated by the dotted line) with respect to the compression direction (indicated by the arrows). (f) Magnified images of the channel intersections in samples LP and HP.

and at heating/cooling rates of 5 K min^{-1}. Two temperature cycles ranged from −60 to 170 °C and phase transformation data were then obtained from the second cycle. The areas under the peaks were used to calculate the enthalpies. The intercepts between the baselines and the tangents at the inflection points of the peaks were taken as the transformation temperatures: A_s, A_p, and A_f refer to austenite-start, -peak, and -finish temperatures, and M_s, M_p, and M_f refer to martensite-start, -peak, and -finish temperatures.

2.4. Mechanical properties characterization

The mechanical properties of the specimens were assessed through compression testing on a screw-driven load frame. Strain was measured by an extensometer

attached to the sample up to ~5%, and by cross-head displacement corrected for machine compliance at higher strains. An alignment cage was used to ensure parallelism of all components. The compression samples were polished with 600 μm grit sand paper to remove surface oxides remaining from the machining process. The specimen then underwent the following heat treatment: (i) annealing for 15 min at 130 °C in air; (ii) air cooling to room temperature with subsequent 20 min hold; (iii) quenching in liquid nitrogen and 3 min hold; and (iv) warming to room temperature and 20 min hold. This ensured that all samples had a martensitic microstructure during compression testing, which was performed at room temperature.

Three types of compressive tests were performed. For each test, a previously untested sample was used. First, to

determine their shape-memory capacities as a function of applied strain load–unload–recovery cycles were performed on specimens LP90, LP45, LP0, HP90, and HP0 at a cross-head speed of 0.05 mm min^{-1}. The specimens were compressed to a maximum strain (ε_{max}) of 1% before being unloaded and taken out of the cage. They were then heat treated as before the test to induce the shape-memory effect. The specimen dimensions were recorded before and after the load–unload cycle and after annealing. The load–unload–recovery cycle was then repeated on the same specimen increasing ε_{max} by 1% for each consecutive cycle, until a load drop was observed. Second, cyclic experiments were performed on specimens HP90 and HP0 to investigate possible changes to the mechanical properties due to repeated deformation and shape-memory recovery, as for actuators. These tests were identical to the load–unload–recovery cycles, except that ε_{max} was constant at 4%, and the test was stopped after six cycles. Third, monotonic compression was performed at a cross-head speed of 0.15 mm min^{-1} on specimens LP90, LP45, LP0, HP90, and HP0 until failure occurred, which was indicated by a sudden reduction in load.

3. Results

3.1. Microstructure

As discussed in Ref. [51], carburization of the coarse mesh was successful: the elevated carbon content resulted in the formation of a ~7 μm thick titanium carbide (TiC) layer at the steel/NiTi interface in composite LP and remained at the channel wall after dissolution of the meshes. This TiC layer prevented the diffusion of iron into the NiTi, resulting in a small average iron content (0.14 wt.%) within the NiTi matrix and Ti-depletion over a ~40 μm thick region adjacent to the channel wall. In composite HP, however, carburization of the fine meshes was unsuccessful and iron diffused into the NiTi matrix. After mesh removal, the iron content in the NiTi matrix peaked at the channel wall and exponentially decayed over a distance of ~40 μm. The average iron content of the NiTi matrix in sample HP was 1.22 wt.% [51].

The average total porosities of specimens LP and HP were 23.7 ± 0.3% (23.3 ± 0.3% open porosity) and 33.5 ± 0.1% (33.4 ± 0.1% open porosity), respectively. The closed porosity of the monolithic control sample was 0.19 ± 0.1%. The morphology of the pores of samples LP and HP can be seen in Fig. 2f, which shows the intersections of elongated channels that are orthogonally interconnected and surrounded by a dense NiTi matrix. The channel diameters are equal to the original wire diameters (i.e., ~350 μm for sample LP and ~400 μm for sample HP). The dimpled channel wall texture results from the steel wires being indented by the NiTi powders during hot-pressing. Since the channel wall of sample LP is lined by a hard TiC layer, the indentation of the NiTi powders is impeded and the dimpling is less severe than in sample HP.

The transformation temperatures and enthalpies of the initial NiTi powder, the monolithic control specimen, and samples LP and HP are listed in Table 1. All hot-pressed samples showed a single-step transformation during heating and cooling [51].

3.2. Monotonic thermo-mechanical properties

Fig. 3 shows the stress–strain curves of all samples under monotonic compression. The compressive strengths (and corresponding strains) for specimens LP0, LP45, and LP90 are 780 MPa (7.8%), 510 MPa (6.4%), and 600 MPa (8.9%), respectively. Specimen HP0 achieves a stress of 720 MPa at 8.1% strain and HP90 reaches a stress of 420 MPa at 7.6% strain. Thus LP0 and HP0 have the highest compressive strengths of all samples and fail at similar strains. LP0 is considerably stronger than LP90 but fails at ~1% lower strain. The high porosity samples exhibit a different behavior, i.e., HP0 fails at a higher stress and strain than HP90. LP45 fails at a lower stress and strain than both LP0 and LP90, since its channels lie in the planes of maximum resolved shear stress.

The load–unload–recovery cycles for all specimens are shown in Fig. 4. Testing was stopped when a load drop was observed. Specimen LP90 survived six cycles, exhibiting a load drop at a strain of 6.5% during the seventh cycle, after which the sample was unloaded again. Specimen HP0 also survived six cycles but failed catastrophically at ~6% strain during the seventh cycle, which is not plotted. All other samples were unloaded after a load drop occurred during the sixth cycle at ~6% strain.

The curves in Fig. 4 were used to calculate loading and unloading stiffness values for each load–unload cycle. Stress values below 20 MPa in the loading regime often showed settling effects, manifested as a concave portion of the stress–strain data. Moreover, non-linearity due to detwinning of the martensite variants sometimes began at stresses as low as ~40 MPa. Thus, for all samples, the loading stiffness was measured as the slope of a best fit line of stress values in the range of 20–40 MPa. The unloading stiffness was measured in the same manner over a 20 MPa interval, starting at σ_{max} – 10 MPa to avoid the stress drop at the onset of unloading resulting from the mechanical hysteresis of the load frame. Fig. 4 clearly shows that the unloading regimes are non-linear at low stresses, indicating that there was some superelastic strain recovery. The stiffness values measured in this fashion contain an estimated error of ±3 GPa. Since martensite detwinning occurs even at low applied stresses due to the stress-concentrating effect of porosity [55], the loading stiffness of porous NiTi measured by compression testing is not a true Young's modulus but rather an effective stiffness. However, the unloading stiffness measured at high stresses is assumed to contain mostly elasticity because the shape-memory effect is thermally (and not stress-)activated and superelastic recovery does not begin immediately upon unloading (resulting in the well-known stress hysteresis in NiTi [40]).

Table 1
DSC results.

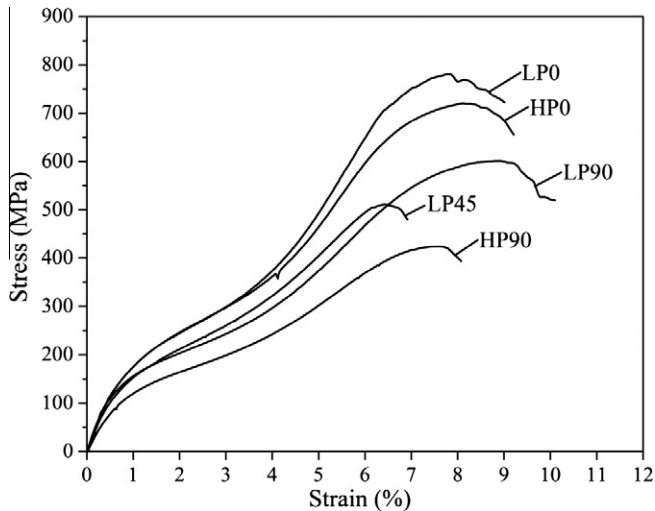| Specimen	Enthalpy (J g^{-1})		Transformation temperatures (°C)					
	Heating	Cooling	A_s	A_p	A_f	M_s	M_p	M_f
Powder	24 ± 0.1	23 ± 0.7	54 ± 0.3	57 ± 0.5	90 ± 0.5	61 ± 0.4	31 ± 0.1	28 ± 0.3
Monolithic	24 ± 0.8	24 ± 1.1	65 ± 1.7	77 ± 2.3	86 ± 1.4	53 ± 1.4	44 ± 0.8	36 ± 0.6
LP	17 ± 0.9	16 ± 1.1	46 ± 3.0	62 ± 2.4	69 ± 2.1	39 ± 1.7	32 ± 1.0	18 ± 3.1
HP	15 ± 0.5	15 ± 0.5	43 ± 2.4	63 ± 3.8	73 ± 1.8	41 ± 1.1	32 ± 2.5	10 ± 1.7

Fig. 3. Compressive stress–strain curves under monotonic loading conditions.

The loading and unloading stiffness are shown as a function of the maximum applied strain in Fig. 5a and b. No trend is observed for the loading stiffness, which remains constant regardless of the prestrain for all samples. The loading stiffness ranged from 21 to 35 GPa, depending on orientation, for the low porosity samples and from 15 to 25 GPa, depending on orientation, for the high porosity samples. At both porosity levels, the loading stiffness measured along the channel plane (0°) exceeded that measured perpendicular to the channel plane (90°) by ~8 GPa. The unloading stiffness values, on the other hand, increase with prestrain, which is particularly pronounced for specimens LP0 and HP0. Since the unloading stiffness values contain only elasticity, they are inherently higher than the loading stiffness (by 7–12 GPa measured for the 1% cycles, which are least affected by prestraining). The monolithic sample had a measured loading stiffness of 65 GPa, which matches previous compression measurements done by extensometry on martensitic NiTi (68 ± 5 GPa [56]).

The maximum applied strains were then separated into four components, as shown in Fig. 6a and b: elastic strain recovery (ε_{el}), superelastic strain recovery (ε_{se}), thermal strain recovery (ε_{rec}), and residual plastic strain (ε_{pl}). The elastic strain was measured by linearly extending the elastic region of the unloading regime to the x-axis and subtracting this x-intercept from the maximum applied strain. The remaining portion of the strain recovered during unloading is the superelastic strain. The difference in strain before and

after heat-treating is the thermal strain recovery resulting from the shape-memory effect. Lastly, the plastic strain was calculated as the difference in strain before testing and after heat-treating. Fig. 6a and b plots the various strain components incrementally against the maximum applied strain during each cycle, and near-linear behavior is observed for all components with no noticeable effect from the loading direction. The elastic and superelastic components are very similar and significantly lower than the thermal recovery. Residual plastic strains remain low until ~4% applied strain. The shape-memory strain recovery, measured as a percentage of the plastic strain remaining after unloading, is shown beneath each cycle in Fig. 4 and ranges from 90% to 97% for the low porosity specimens and from 86% to 94% for the high-porosity specimens (disregarding the first and last cycles for each sample, which have higher errors).

3.3. Cyclic thermo-mechanical properties

The thermo-mechanical response of samples HP90 and HP0 under cyclic loading is shown in Fig. 7a and b. The accumulation of residual plastic strain causes a shift along the x-axis after each load–unload–recovery loop, which is greatest after the first cycle and diminishes thereafter.

Fig. 8a shows the various components of the strain (normalized by the maximum applied strain) plotted incrementally as a function of cycle number. For both samples, the plastic strain accumulated after each cycle decreases with cycle number, most strongly after the first cycle. For specimen HP0, the plastic strain is completely eliminated after the third cycle. For specimen HP90 the same is achieved after the fifth cycle. An increase in thermal recovery is noted, particularly after the first cycle, but levels off after three cycles. Sample HP0 shows higher superelastic recovery and slightly lower thermal and elastic recoveries than sample HP90.

The loading and unloading stiffness is measured as described above for each cycle and plotted against the cycle number in Fig. 8b. For both specimens, no trend is observed in the loading and unloading stiffness. The average loading stiffness values of specimens HP90 and HP0 are 16 and 22 GPa, respectively. The average unloading stiffness of specimen HP90 is 28 GPa, while that of specimen HP0 is significantly greater at 46 GPa.

Figs. 7 and 8 demonstrate that no degradation occurs in recovery strains, stiffness, or the shape of the stress–strain curve during cyclic loading, apart from the initial change after the first cycle.
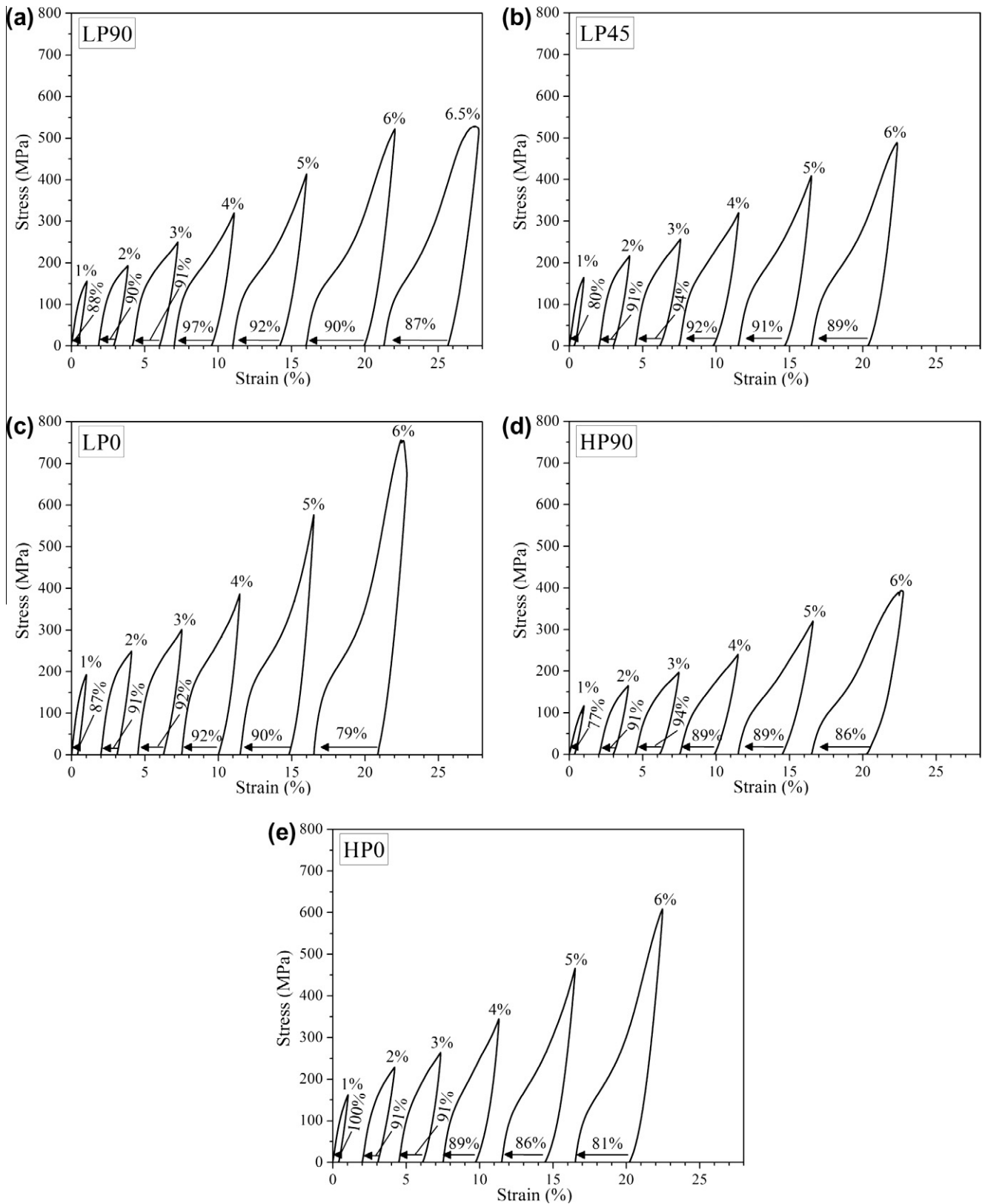
Fig. 4. Compressive load–unload–recovery cycles for samples (a) LP90 [51], (b) LP45, (c) LP0, (d) HP90 [51], and (e) HP0. The individual cycles have been shifted along the x-axis for clarity. The numbers above the individual cycles indicate the maximum applied strain. The arrows indicate the percentage of the total plastic strain that is recovered after heating above A_f.
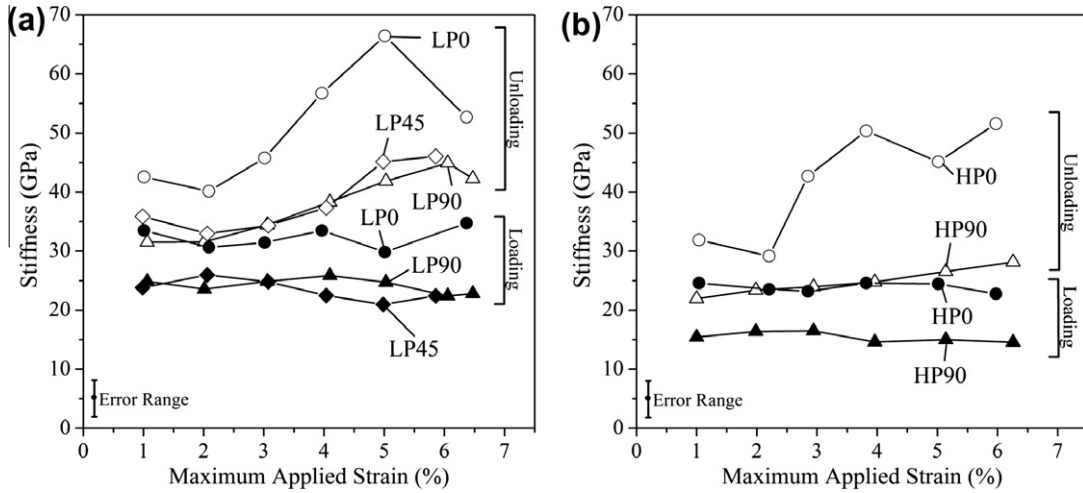
Fig. 5. Loading and unloading stiffness as a function of maximum applied strain for various orientations of (a) LP and (b) HP samples.
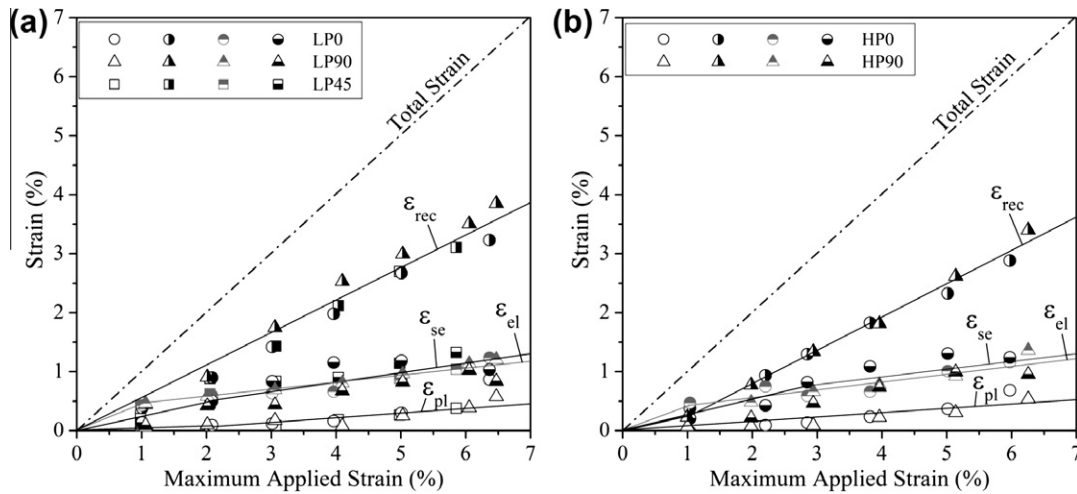

Fig. 6. Incremental elastic recovery (ε_{el}), superelastic recovery (ε_{se}), thermal recovery (ε_{rec}), and plastic strain (ε_{pl}) as a function of maximum applied strain for various orientations of (a) LP and (b) HP samples.
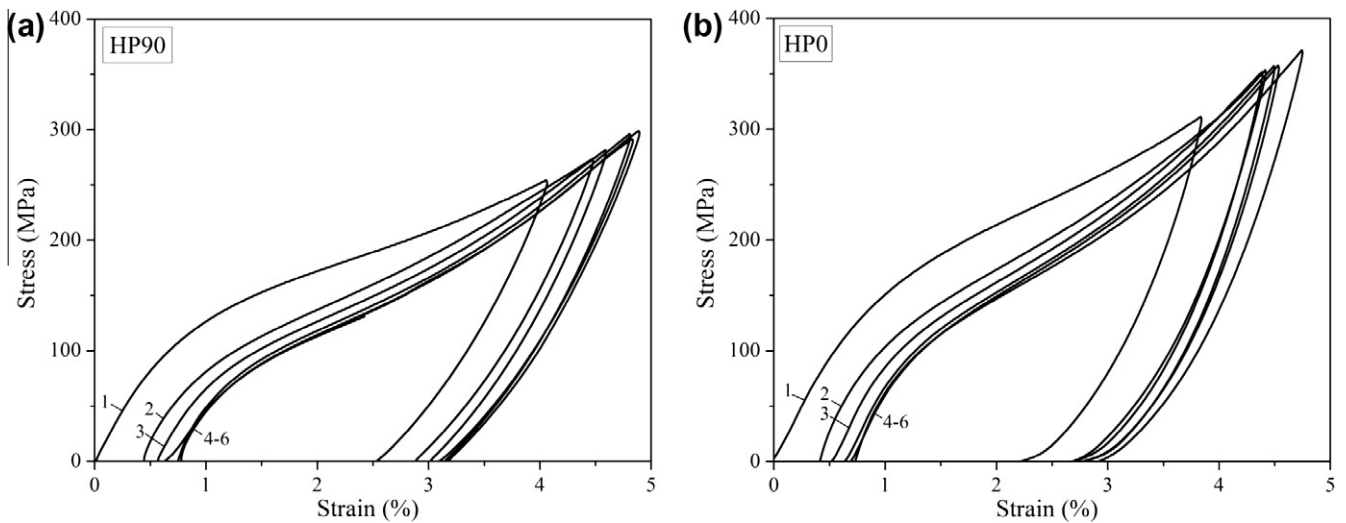

Fig. 7. Compressive curves of sample (a) HP90 and (b) HP0, as the load–unload–recovery cycle number increases from 1 to 6 (as indicated). Unlike Fig. 4, the individual cycles have not been shifted along the x-axis, so accumulation of plastic strain is directly visible on the x-axis.
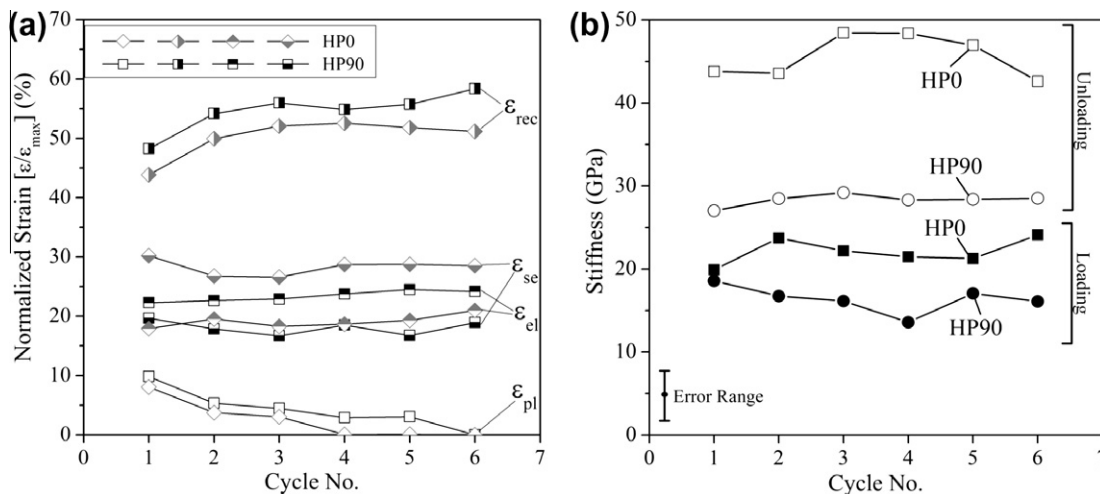
Fig. 8. (a) Elastic recovery (ε_{el}), superelastic recovery (ε_{se}), thermal recovery (ε_{rec}), and plastic strain (ε_{pl}) normalized by the maximum applied strain (ε_{max}), shown incrementally as a function of cycle number for samples HP90 and HP0. (b) Loading and unloading stiffness as a function of cycle number for samples HP90 and HP0.

4. Discussion

4.1. Processing and structure

Full powder densification is achieved by applying a uniaxial pressure of 60 MPa during sintering. This is significantly better than pressureless sintering for 3 h at 1050 °C, after which ∼10% closed porosity remains, resulting in reductions in strength and ductility [16]. The channels in the present samples are orthogonally interweaving and aligned in separate parallel layers (Fig. 2), replicating precisely the initial space-holder meshes (Fig. 1b and c). Other geometries could easily be created by utilizing a space-holder with a different shape, allowing for the creation of intricate pore architectures.

Most of the NiTi foaming techniques discussed in the Introduction are limited to creating equiaxed and randomly or uniformly distributed pores resulting in isotropic material properties, with the exception of continuous zone melting [10,11] and SHS [41–45,57–59]. LENS is capable of closely controlling the macropore geometry and was recently used to fabricate titanium foams with elongated and aligned channels [47], and could thus also be applied to NiTi. However, the steel space-holder technique described here is the first to simultaneously permit (i) tailoring the pore volume, morphology, distribution, and orientation, (ii) full densification of the NiTi matrix, and (iii) close control over the matrix composition by using prealloyed NiTi powders. Concerning the last point the following results from Ref. [51] should be reiterated: specimens LP and HP show composition changes near the channels due to titanium depletion to create a TiC layer in specimen LP and due to Fe diffusion into the NiTi matrix in specimen HP. Despite these compositional differences between the two types of samples, no adverse effects on the thermo-mechanical properties of the specimens were observed, as both exhibited very similar shape-memory and superelastic behavior and high strengths. In Ref. [51], it was shown that the volume fractions of non-transforming material are the same for both LP (due to TiC formation) and HP (due to Fe contamination), and that the corresponding effects on the thermomechanical properties are very similar. Thus, differences in thermo-mechanical properties between the LP and HP samples can be attributed solely to differences in porosities. Reduction in transformation temperatures and enthalpies in the porous samples compared with the monolithic control (Table 1) was explained by their composition gradients at the channel walls [51], since porosity does not affect the DSC behavior [37,38].

The average steel dissolution time of composites LP (all mesh orientations) was 47 h while that of composites HP (all mesh orientations) was only 35 h, despite the significantly higher volume fraction of steel in the latter (∼34% in HP compared with ∼24% in LP). This is caused by a superior accessibility for fresh electrolyte to penetrate deep into the material in specimen HP compared to specimen LP, which results from the larger wire diameter and higher number of fenestrations between orthogonal wires, increasing transport of electrolyte and corrosion products to and from the reaction sites. The average material removal rates (MRR) of the space-holders in specimens LP and HP (all orientations) were 1.3 and 2.3 mm^3 h^{-1}, respectively. Thus, for these samples, the present technique produces orthogonal micro-channels much faster than EDM, which is capable of producing individual micro-holes of comparable size in NiTi at an MRR of ∼0.34 mm^3 h^{-1} [60]. This is explainable by the inherently parallel nature of the present process, by which multiple channels can be formed simultaneously so that the total MRR can be increased easily, e.g.

by dissolving multiple samples electrically connected with each other.

4.2. Thermo-mechanical and shape-memory properties

4.2.1. Maximum strength

The compressive strength at both porosity levels was highest when loading was applied parallel to the channel orientation (i.e., samples LP0 and HP0, Fig. 3). This behavior has previously been documented in titanium [12] and iron [61] foams with elongated pores as well as lamellar metal/ceramic composites [62]. Moreover, the compressive strength and strain of LP45 are the lowest of all low porosity samples, which can be explained by the alignment of its pores along the direction of the maximum resolved shear stress (i.e., at 45° to the loading direction). However, even LP45 shows a higher compressive strength than a martensitic foam produced by HIP densification with NaF equiaxed powder space-holders that had 20% total porosity (with 6.6% closed porosity due to incomplete densification) and failed at a stress of 480 MPa [37]. Thus the improved powder densification during hot-pressing compensated for the reduction in strength at 45° to the channel direction.

LP0 has a slightly higher porosity (24.5%) than LP90 (23.7%), while HP90 has a slightly higher porosity (33.7%) than HP0 (31.8%), which may explain why LP0 has a lower compressive strain than LP90 while HP0 has a greater compressive strain than HP90. The failure strains discussed here are associated with the first load drop and are not equivalent to densification strains. Contrary to conventional ductile foams with equiaxed pores, there is no large-scale densification stage in the stress–strain response of the present samples, which fracture shortly after the failure strain is reached. In foams where densification occurs, there is a linear relationship between porosity and densification strain [63].

By comparing HP90 with HP0 and LP90 with LP0, it can be deduced that the effect of channel orientation on the compressive strength is greater at 34% porosity than at 24% porosity. Conversely, comparing HP90 with LP90 and HP0 with LP0 shows that a sample with channel planes aligned along the loading direction (0°) is less affected by the pore volume fraction than one with channel planes aligned perpendicular to the loading direction (90°).

4.2.2. Stiffness

The unloading stiffness increases as a function of pre-strain (see Fig. 5), while the loading stiffness remains fairly constant for all specimens. This trend was previously documented for NiTi foams fabricated by HIP densification with NaCl space-holders [38] and can be attributed to the purely elastic nature of the unloading stiffness, which increases at high strains due to slight densification or plastic deformation of the micro-channels. Upon loading, however, elasticity, plasticity, and detwinning of the martensite variants occur simultaneously in the linear part of the stress–strain curve with a concomitant decrease in the effective stiffness.

These three influences have not been decoupled in the present work. In LP0 and HP0, the increase of the unloading (elastic) stiffness is greater than for the other samples. This may indicate that the layers of orthogonally interweaving channels in the specimens are most prone to collapsing (i.e., densifying) from loading in the in-plane directions.

Ref. [51] discusses the stiffness values of LP90 and HP90 by comparing to previously published results of NiTi foams with similar levels of equiaxed porosities. These equiaxed foams are less stiff than specimens LP90 and HP90, which is believed to result from the alignment of the channels and reduced stress concentrations that can trigger detwinning. In the present work, the loading stiffness values along the directions of the porous planes (i.e., from LP0 and HP0) are found to be ∼8 GPa greater than perpendicular to the porous planes, representing a 33% and 52% increase in stiffness from specimens LP90 and HP90, respectively. Thus, the micro-channel orientation provides an additional degree of freedom for tailoring the material stiffness.

4.2.3. Strain recovery

As discussed in Ref. [51], the strain recovery behaviors of samples LP90 and HP90 are very similar. Fig. 6 plots the four components of the unloading strain (elastic, superelastic, thermal, and plastic) as a function of the maximum strain applied during each unload cycle. The loading direction has no significant effect on the four strain components which increase with maximum applied strain in a near-linear fashion. This linear behavior visible in Fig. 6 is not expected to extend far beyond the highest applied strain of 6.5% used here, because the maximum strain recoverable by shape-memory or superelasticity is ∼8% in NiTi [40]. Furthermore, the elastic strain recovery, which is proportional to the stress, is also expected to level off, so that, at high applied strains (>10%), the plastic component will dominate. At low applied strains (<1%), the elastic strain recovery becomes dominant, since a critical stress needs to be reached for the other strain components (plastic deformation, detwinning or stress-induced martensite formation). Similar results were demonstrated for isotropic NiTi foams produced by HIP-densification around NaCl [38] and NaF [37] space-holders, where the unloading strains (sum of elasticity and superelasticity) exceeded the shape-memory strains at low applied strains. However, the individual elastic and superelastic strain recovery components were not reported.

The total percentage recovered (i.e., the sum of elastic, superelastic, and thermal strains) for a maximum applied strain of 5% ranges from 94% to 95% for LP and from 93% to 94% for HP. Evidently, the presence of non-transforming phases (TiC and (Ni,Fe)Ti) does not significantly reduce the shape-memory effect regardless of the loading direction, which agrees with results obtained for NiTi/TiC composites that retained a high shape-memory despite the presence of 10 vol.% TiC [64]. From Fig. 6, it is apparent that the strain recovery is not only caused by shape-memory and

superelasticity but also by elasticity, by which ∼1% strain was recovered. Again, this is true for all loading directions.

4.2.4. Cyclic loading

Fig. 8a, which plots the strain components incrementally against the cycle number, shows that the plastic strain remaining after each load–unload–recovery cycle decreases with cycle number for both HP90 and HP0, resulting in cyclic stress–strain cycles that begin to overlap after approximately four cycles (Fig. 7a and b). This decrease in residual plastic strain between consecutive cycles has previously been documented in monolithic martensitic NiTi subjected to symmetric tension–compression cycles that were strain-controlled to 9% applied strain [65]: an initial decrease in plastic strain increment and increase in shape-memory recovery strain increments was followed by a regime where these strains remain constant with cycle number. However, due to the magnitude of the applied strain (9%), there was no complete elimination of the plastic strain increment. The incremental elastic recovery strains remained constant throughout, which matches the results presented here for porous NiTi (Fig. 8a). Insensitivity of the incremental plastic strain to cycle number at higher load cycles has also been documented in superelastic NiTi [66,67] and has been attributed to the introduction of dislocations during cycling that cause work hardening [67].

No trend is observed for the loading stiffness as a function of cycle number (Fig. 8b). Contrary to the results obtained from incrementally increasing prestrain (Fig. 5), no trend is observed for the unloading stiffness as a function of cycle number either. This result is expected because densification that leads to residual plastic strain should occur only in the first cycle. The average loading and unloading stiffnesses of HP90 (16 and 28 GPa, respectively) are within error of the loading and unloading stiffness of HP90 after the 4% strain cycle shown in Fig. 5 (15 and 25 GPa, respectively). Likewise in sample HP0, the average loading and unloading stiffnesses (22 and 46 GPa, respectively) are close to the loading and unloading stiffnesses measured during the 4% strain cycle in Fig. 5 (25 and 50 GPa, respectively).

4.3. Stiffness models

Plots of loading and unloading stiffness values vs. porosity are given for samples LP90 and HP90 in Fig. 9a and samples LP0 and HP0 in Fig. 9b. For specimens at both porosity levels, only the first load–unload–recovery cycle was used to obtain loading and unloading stiffness, so that the effect of prestraining is minimal. Two additional loading stiffness values are obtained for high-porosity specimens (HP90 and HP0) from the first load cycle in Fig. 7 and the monotonic compression test (Fig. 3). The unloading stiffness values are expected to be primarily elastic and can thus be compared against various models for the Young's modulus of foams, as described below.

In the ensuing discussion, the stiffness values are labeled $E^{(90)}$, $E^{(45)}$, or $E^{(0)}$ to distinguish between the 90°, 45°, and

0° orientation of the porous layers with respect to the compressive stress (referring to specimens LP90/HP90, LP45, and LP0/HP0, respectively). Moreover, p refers to the total porosity and E_m is the matrix (bulk) stiffness, measured to be 65 GPa in compression testing of the monolithic control sample (Section 3.2).

4.3.1. Gibson–Ashby foam model

The Gibson–Ashby model was derived for isotropic foams with equiaxed cells which deform by strut bending [68] but is known to apply for other pore geometries as well. The foam Young's modulus E is related to the Young's modulus of the bulk material E_m by:

$$\frac{E}{E_m} = C\left(\frac{\rho}{\rho_m}\right)^2 \tag{1}$$

where ρ and ρ_m are the foam and matrix (bulk) densities respectively, and C is a geometric constant taken to be unity. The relative density is related to the dimensionless foam porosity by $\rho/\rho_m = 1 - p$.

As shown in Fig. 9, the model overestimates the unloading stiffness at both porosity levels by ∼6 GPa in the 90° direction. In the 0° direction it underestimates the unloading stiffness at both porosity levels by ∼4 GPa. Lastly, the model overestimates the stiffness of specimen LP45 in the 45° direction by 3 GPa. Given the very different geometric assumptions made in the model, its predictions, at least for the present volume fractions, are surprisingly close to the data and can be used as a first approximation.

4.3.2. Mori–Tanaka fiber model

The Mori–Tanaka fiber model, based on Eshelby's elasticity solution for inclusions in an infinite medium, is used for composites with aligned cylindrical inclusions and extended to the present porous specimens by setting the inclusion stiffness to zero. The compliance tensor S of the specimen is given by [69,70]:

$$S = C_m^{-1} - p((C_f - C_m)(S_{cyl} - p(S_{cyl} - I)) + C_m)^{-1}$$
$$(C_f - C_m)C_m^{-1} \tag{2}$$

where C_m is the elastic stiffness tensor of NiTi (determined using a Young's modulus of 65 GPa, a Poisson's ratio of 0.3 [54], and the assumption of isotropy for bulk NiTi), C_f is the stiffness tensor of the inclusions (taken as zero), S_{cyl} is the Eshelby tensor describing cylindrical inclusions, and I is the identity matrix. Solving this equation, stiffnesses are found, in reduced index notation, as $E^{(90)} = 1/S_{11}$ and $E^{(0)} = 1/S_{33}$, since the 11 and 33 matrix elements refer to the radial and axial directions, respectively. To calculate $E^{(45)}$, a 45° rotation of the matrix $[S]$ about the 2-axis was performed by solving $[S'] = [R][S][R]^T$, where $[S']$ is the rotated compliance matrix and $[R]$ is the rotation matrix. Then, $E^{(45)} = 1/S'_{33}$.

The Mori–Tanaka model overestimates the 90° unloading stiffness by ∼4 GPa at both porosity levels. In the 0° direction, the unloading stiffness is overestimated by
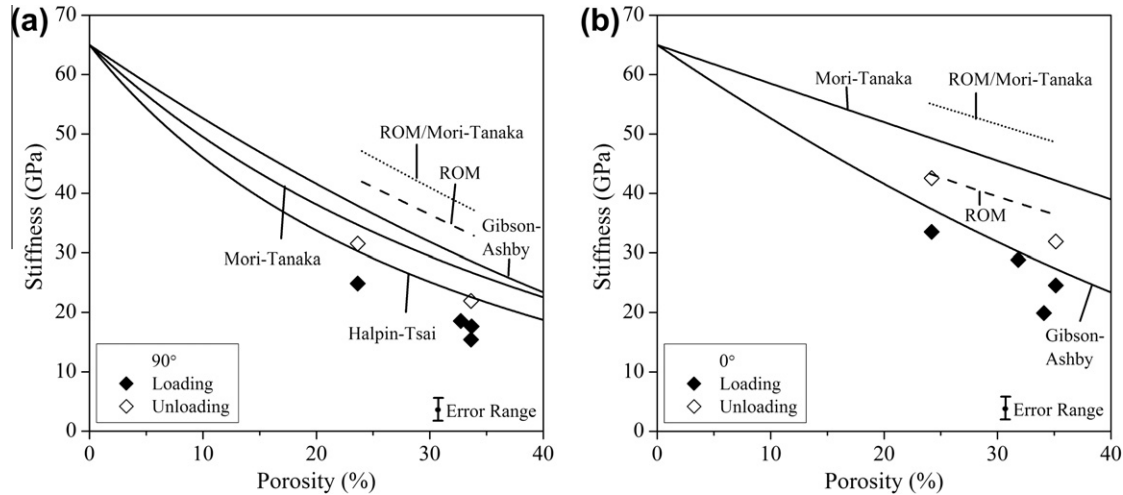
Fig. 9. Loading and unloading stiffness as a function of porosity for samples loaded (a) perpendicular (90°) and (b) parallel (0°) to the channel orientation. The following foam and composite model predictions are plotted for comparison: Gibson–Ashby (Eq. (1)); Mori–Tanaka (Eq. (2)); Halpin–Tsai (Eq. (3)); ROM (Eq. (4)); and ROM/Mori–Tanaka (Eq. (6)).

$\sim$8 GPa at both porosity levels. In both cases, the model is expected to provide an overestimate for the stiffness [71]. Furthermore, this model applies to the case where all micro-channels are aligned in the loading direction, which is not true for the present transversely isotropic specimens, so that the predicted stiffness is expected to be overestimated. After a 45° rotation, the predicted stiffness at low porosity is 40.0 GPa, which slightly overestimates the unloading stiffness of 35.7 GPa measured on sample LP45.

4.3.3. Halpin–Tsai composite model (90°)

Halpin and Tsai proposed a semi-empirical model that is widely used to predict the transverse stiffness $E^{(90)}$ of aligned fiber composites [69]:

$$E^{(90)} = E_m \frac{1 + \xi\eta p}{1 - \eta p} \tag{3}$$

with $\eta = (E_f/E_m - 1)/(E_f/E_m + \xi)$. Here E_f is the fiber Young's modulus and is equal to zero for the present porous specimens, so $\eta = -1/\xi$. The adjustable parameter ξ was set to 0.37, since this provided the closest fit with measured unloading stiffness values. This model, which is most accurate for large and small fiber volume fractions [69], predicts a Young's modulus of the present 90° specimens that is within error at both high and low porosities.

4.3.4. Rule-of-mixtures models (90°, 0°)

A simplified approach to model a laminar composite is to treat it as several slabs bonded together, each exhibiting its own volume fraction of reinforcement and stiffness. The present porous NiTi samples lend themselves to this approach because they have a structure reminiscent of laminar composites, i.e., solid layers alternating with porous layers.

The samples are best divided into three slabs: one to represent the matrix and two to represent the layers of orthogonal micro-channels (see Fig. A1, Appendix A). Using a rule-of-mixtures (ROM) approach, the following approximations for $E^{(90)}$ and $E^{(0)}$ are obtained (a derivation is given in Appendix A):

$$E^{(90)} = E_m \left(1 + \frac{p}{f}\right)^{-1} \tag{4a}$$

$$E^{(0)} = E_m \left(1 - \frac{p}{1-f} + \frac{fp}{2(1-f)}\right) \tag{4b}$$

where f is the volume fraction of solid material in the porous layers and p is, as before, the total porosity. Since the micro-channels are simplified as square prisms (Fig. A1), f is approximately equal to the open area of the space-holder meshes.

To eliminate f from the above equations, a linear relationship between p and f is assumed:

$$f = \frac{p - p_{LP}}{p_{HP} - p_{LP}}(f_{HP} - f_{LP}) + f_{LP} \tag{5}$$

Here, $p_{LP} = 0.237$ and $p_{HP} = 0.335$ are the total porosities of the two specimens, and f_{LP} and f_{HP} are measured from Fig. 1b and c as 0.44 and 0.35, respectively. This result for the fine mesh is slightly different than the nominal open area fraction (0.27, Section 2.2). Eqs. (4a) and (5) (the latter in a different but equivalent form) were used in Ref. [50] to predict the stiffness of Ti–6Al–4V structures with similar micro-channels as in the present specimens. Since the assumption of linearity made in Eq. (5) only holds for porosities similar to those of the present specimens ($\sim$24–34%), solutions to the ROM-based models are only plotted over this porosity range in Fig. 9.

The Young's moduli calculated from the ROM model overestimate the unloading stiffness of the 90° specimens by $\sim$10 GPa at both porosities. For the 0° specimens, the model correctly predicts the low porosity stiffness, but again overestimates the high porosity stiffness by $\sim$5 GPa. The

micro-channels in the ROM model for the 90° specimens are all perpendicular to the loading direction, which is in fact true for the present samples (see Fig. A1). In the 0° ROM model, however, it is assumed that half of the micro-channels are parallel and half are perpendicular to the loading direction. In reality the channels are rotated isotropically in the planes of the porous layers so that most of them are oriented between 0° and 90° to the loading axis. Thus, if the micro-channels can truly be approximated as square prisms, the stiffness values predicted for the 90° specimens are expected to be more accurate than those predicted for the 0° specimens. Since this is contrary to the results shown in Fig. 9, it is clear that the micro-channel geometry must be better accounted for in more complex models.

4.3.5. ROM/Mori–Tanaka model

To account for both the micro-channel alignment and geometry, the Mori–Tanaka approach is used to calculate the Young's moduli in the two porous layers, which are then related to the total Young's modulus by the ROM models. By this method, the Young's modulus along the 45° direction can also be approximated, which was not possible using pure ROM models. As derived in Appendix A, $E^{(90)}$, $E^{(0)}$, and $E^{(45)}$ are given by:

$$E^{(90)} = E_m \left[1 - \frac{p}{1-f} \left(1 + E_m S_{11} \right) \right]^{-1} \tag{6a}$$

$$E^{(0)} = E_M \left[1 - \frac{p}{1-f} \left(1 + \frac{1}{2E_m} \left(\frac{1}{S_{11}} + \frac{1}{S_{33}} \right) \right) \right] \tag{6b}$$

$$E^{(45)} = E_m \left[1 - \frac{p}{1-f} \left(1 + \frac{E_m(S_{11} + S'_{33})}{2} \right) \right]^{-1} \tag{6c}$$

where S_{11}, S_{33}, and S'_{33} are defined in Section 4.3.2. Furthermore, f is again given by Eq. (5), so the validity of these models is also confined to the porosity range of the present samples.

In the 90° direction, this combined ROM/Mori–Tanaka model predicts Young's moduli greater than those predicted by the individual ROM and Mori–Tanaka models, indicating that the errors of both models are compounded in this direction, resulting in an overestimation of the unloading stiffness by ~15 GPa. Improvements are expected for models that account for the isotropic rotation and interweaving morphology of the channels.

In the 0° direction, the ROM/Mori–Tanaka model gives the highest values of all presented models. This is because, while the ROM model assumes a stiffness of zero in the layer with channels oriented at 90° to the load direction (i.e., layer 2 in Fig. A1 presented in Appendix A), the ROM/Mori–Tanaka model assumes a non-zero stiffness in this same layer, corresponding to the stiffness of a composite with fibers oriented at 90° to the loading direction. As seen for the 90° direction, the inability of this model to accurately predict the stiffness suggests that even the cylindrical channel geometry assumed by the Mori–Tanaka model is a significant oversimplification of the interweaving

channels in the present specimens. In the 45° direction, the ROM/Mori–Tanaka prediction (36.3 GPa) closely approximates the measured unloading stiffness (35.7 GPa) for specimen LP45.

In summary, within the porosity range of 24–34%, the above simplified foam and composite models can provide approximate values for the stiffness of the present samples despite the complex architecture of the micro-channels. Comparison with experimental data is complicated by the fact that the unloading stiffnesses, assumed here to be purely elastic, may in fact underestimate the Young's modulus (albeit less so than on loading) due to strain contributions from plasticity and detwinning. For modeling the mechanical properties of shape-memory porous alloys, particularly those with a complex geometry of pores, it is often best to utilize a finite element (FE) approach [50,72], since FE can account for non-linear material behavior as well as complex internal architectures and stress concentrations. In fact, FE calculations were performed for Ti–6Al–4V samples, with similar architecture and volume fractions (19% and 34%) of micro-channels created by the same method (electro-dissolution of steel space-holder meshes) in Ref. [50]; the stiffness values predicted by FE were almost identical to those predicted by the Gibson–Ashby model, illustrating that simplified models sometimes suffice in characterizing complex structures.

5. Conclusions

The thermo-mechanical properties of nickel–titanium (NiTi) alloys, with parallel layers of orthogonally interweaving 350–400 μm diameter micro-channels fabricated by a replication method, are investigated as a function of loading angle by compression testing and subsequent shape-memory heat treatments.

Depending on the loading direction, loading stiffness values of 21–35 GPa are measured for specimens with 24% porosity, and of 15–25 GPa for specimens with 34% porosity. The highest stiffness is achieved when the loading direction is aligned with the porous layers and the lowest when loaded perpendicular to the porous layers. The stiffness values are compared to several foam and composite models that, despite their greatly simplifying geometric assumptions, predicted reasonably accurate values useful for a first approximation.

The thermo-mechanical response of the porous NiTi, when loaded repeatedly to 4% strain, quickly approaches a steady-state, such that the shape of the stress–strain curve, the stiffness, and the strain recovery remain unaffected by the number of cycles. Over the first three to five cycles the irrecoverable plastic deformation goes to zero, resulting in complete shape recovery for subsequent cycles.

The strain recovery is unaffected by the loading direction: by a combination of elasticity and superelasticity on unloading and shape-memory on heating, the vast majority (93–98%) of an applied strain up to 6% can be recovered for both low and high porosity samples.

The mechanical and shape-memory properties of these porous NiTi structures – combined with the versatility in the channel geometries that can be fabricated by the present method – make them attractive for various applications, including bone implants, actuators, and energy absorbers.

Appendix A

A.1. Derivations of the ROM models

A.1.1. General considerations

Let v_1, v_2, and v_3 be the volume fractions of layers 1, 2, and 3, respectively (Fig. A1). Since the sum of these volume fractions is unity and layers 2 and 3 are identical (except for the channel orientation), we obtain:

$$v_1 = 1 - 2v_3 \tag{A1a}$$

$$v_2 = v_3 \tag{A1b}$$

$$v_3 = \frac{p}{2(1-f)} \tag{A1c}$$

where $1 - f$ is the porosity in layers 2 and 3. Eq. (A1) hold for all models derived hereafter. Moreover, since layer 1 is bulk NiTi, $E_1 = E_m$ for all models.

A.1.2. ROM model

Rule-of-mixtures Reuss and Voigt equations for $E^{(90)}$ and $E^{(0)}$ are given by [69]:
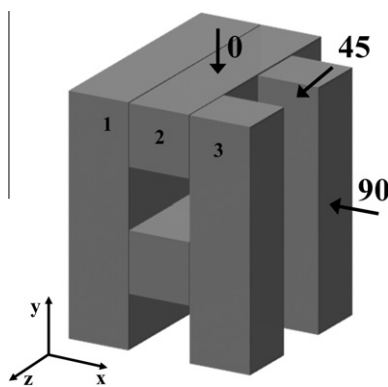

Fig. A1. Schematic unit cell of the simplified three-layer architecture assumed for the ROM and ROM/Mori–Tanaka models. The three relevant loading directions are indicated by the arrows and the three layers are labeled as 1, 2, and 3.
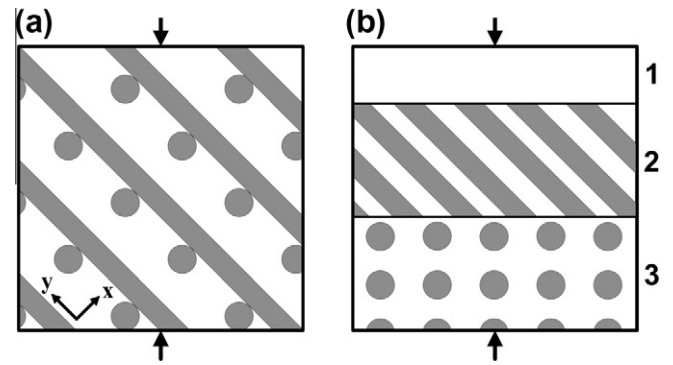

Fig. A2. (a) Side view of the simplified architecture assumed in the ROM/Mori–Tanaka model for specimen LP45, showing schematically two types of wires: those inclined at 45° to the loading direction (indicated by the grey stripes) and those aligned perpendicular to the loading direction (indicated by the grey circles). (b) Further simplification, dividing the specimen into the three separate layers used in the ROM/Mori–Tanaka model. The arrows indicate the loading direction.

$$E^{(90)} = \left(\frac{v_1}{E_1} + \frac{v_2}{E_2} + \frac{v_3}{E_3} \right)^{-1} \tag{A2a}$$

$$E^{(0)} = v_1 E_1 + v_2 E_2 + v_3 E_3 \tag{A2b}$$

Eqs. (A2a) and (A2b) are applicable when the layers are aligned in series and in parallel, respectively, with respect to the loading direction. In the 90° direction, both layers 2 and 3 carry the same amount of load, and the Young's moduli are estimated as $E_2 = E_3 = f * E_m$, which is itself a Voigt model assuming a channel stiffness of zero. Substituting these values of $E_2 = E_3$ and Eqs. (A1) into Eq. (A2a) produces Eq. (4a). In the 0° direction, no load is carried by layer 2 such that $E_2 = 0$ and $E_3 = f * E_m$. Substituting these values and Eqs. (A1) into Eq. (A2b) produces Eq. (4b).

A.1.3. ROM/Mori–Tanaka model

The Young's moduli for layers 2 and 3 are now given by the solutions to the Mori–Tanaka Equation (Eq. (2)). In the 90° perpendicular direction, the micro-channels in layers 2 and 3 are all normal to the load, so $E_2 = E_3 = 1/S_{11}$. Substituting this and Eq. (A1) into Eq. (A2a) produces Eq. (6a). In the 0° direction, the micro-channels of layers 2 and 3 are aligned perpendicular and parallel to the applied load, respectively. Thus $E_2 = 1/S_{11}$ and $E_3 = 1/S_{33}$. Substituting these and Eqs. (A1) into Eq. (A2b) produces Eq. (6b).

Lastly, in the 45° direction, Eq. (A2a) applies because the three layers are stacked in series with respect to the applied load (see Fig. A2b). The micro-channels of layer 2 are aligned at 45° (in the x–y plane shown in Figs. A1–A2) while those of layer 3 are perpendicular to the applied load. Thus $E_2 = 1/S'_{33}$ and $E_3 = 1/S_{11}$. Substituting these and Eqs. (A1) into Eq. (A2a) produces Eq. (6c).

References

[1] Elzey DM, Sofla AYN, Wadley HNG. Int J Solids Struct 2005;42:1943.

[2] Ayers RA, Simske SJ, Bateman TA, Petkus A, Sachdeva RLC, Gyunter VE. J Biomed Mater Res 1999;45:42.

[3] Bansiddhi A, Sargeant TD, Stupp SI, Dunand DC. Acta Biomater 2008;4:773.

[4] Rhalmi S, Odin M, Assad M, Tabrizian M, Rivard CH, Yahia LH. Biomed Mater Eng 1999;9:151.

[5] Zhu SL, Yang XJ, Chen MF, Li CY, Cui ZD. Mater Sci Eng C: Biomimetic Supramolec Sys 2008;28:1271.

[6] Muhammad AQ, Virginia GD. Smart Mater Struct 2004;13:134.

[7] Zhao Y, Taya M, Izui H. Int J Solids Struct 2006;43:2497.

[8] Lagoudas DC, Vandygriff EL. ASME/ASCE/SES joint summer meeting; 2001. p. 837.

[9] Tane M, Ichitsubo T, Nakajima H, Hyun SK, Hirao M. Acta Mater 2004;52:5195.

[10] Sugiyama M, Hyun SK, Tane M, Nakajima H. High Temp Mater Process 2007;26:297.

[11] Nakajima H. Prog Mater Sci 2007;52:1091.

[12] Spoerke ED, Murray NGD, Li H, Brinson LC, Dunand DC, Stupp SI. J Biomed Mater Res A 2008;84A:402.

[13] Chino Y, Dunand DC. Adv Eng Mater 2009;11:52.

[14] Hakamada M, Asao Y, Kuromura T, Chen Y, Kusuda H, Mabuchi M. Scripta Mater 2007;56:781.

[15] Lagoudas DC, Entchev PB, Vandygriff EL. Smart structures and materials conference; 2002. p. 224.

[16] Yuan B, Zhang XP, Chung CY, Zeng MQ, Zhu M. Metall Mater Trans A, Phys Metall Mater Sci 2006;37A:755.

[17] Bertheville B. Biomaterials 2006;27:1246.

[18] Sadrnezhaad SK, Arami H, Keivan H, Khalifezadeh R. Mater Manuf Process 2006;21:727.

[19] Sadrnezhaad SK, Hosseini SA. Mater Des 2009;30:4483.

[20] Panigrahi BB, Godkhindi MM. Intermetallics 2006;14:130.

[21] Zhu SL, Yang XJ, Fu DH, Zhang LY, Li CY, Cui ZD. Mater Sci Eng A 2005;408:264.

[22] Zhu SL, Yang XJ, Hu F, Deng SH, Cui ZD. Mater Lett 2004;58:2369.

[23] Grummon DS, Shaw JA, Gremillet A. Appl Phys Lett 2003;82:2727.

[24] Zhao Y, Taya M, Kang YS, Kawasaki A. Acta Mater 2005;53:337.

[25] Hosseini SA, Sadrnezhaad SK, Ekrami A. Mater Sci Eng C 2009;29:2203.

[26] Greiner C, Oppenheimer SM, Dunand DC. Acta Biomater 2005;1:705.

[27] Yuan B, Zhu M, Gao Y, Li X, Chung CY. Smart Mater Struct 2008;17:7.

[28] Oppenheimer SM, Dunand DC. Mater Sci Eng A 2009;523:70.

[29] Köhl M, Habijan T, Bram M, Buchkremer HP, Stöver D, Köller M. Adv Eng Mater 2009;11:959.

[30] Hu GX, Zhang LX, Fan YL, Li YH. J Mater Process Technol 2008;206:395.

[31] Bansiddhi A, Dunand DC. J Mater Res 2009;24:2107.

[32] Bansiddhi A, Dunand DC. J Mater Eng Perform, submitted for publication. doi:10.1007/311665-010-9827-6.

[33] Li DS, Zhang YP, Ma X, Zhang XP. J Alloys Compd 2009;474:L1.

[34] Wu S, Chung CY, Liu X, Chu PK, Ho JPY, Chu CL, et al. Acta Mater 2007;55:3437.

[35] Xiong JY, Li YC, Wang XJ, Hodgson PD, Wen CE. J Mech Behav Biomed Mater 2008;1:269.

[36] Aydogmus T, Bor S. J Alloys Compd 2009;478:705.

[37] Bansiddhi A, Dunand DC. Intermetallics 2007;15:1612.

[38] Bansiddhi A, Dunand DC. Acta Biomater 2008;4:1996.

[39] Zhao X, Sun H, Lan L, Huang J, Zhang H, Wang Y. Mater Lett 2009;63:2402.

[40] Otsuka K, Ren X. Prog Mater Sci 2005;50:511.

[41] Wisutmethangoon S, Denmud N, Sikong L. Mater Sci Eng A, Struct Mater, Prop Microstruct Process 2009;515:93.

[42] Tay BY, Goh CW, Gu YW, Lim CS, Yong MS, Ho MK, et al. J Mater Process Technol 2008;202:359.

[43] Li BY, Rong LJ, Li YY, Gjunter VE. Acta Mater 2000;48:3895.

[44] Kim JS, Kang JH, Kang SB, Yoon KS, Kwon YS. Adv Eng Mater 2004;6:403.

[45] Yeh CL, Sung WY. J Alloys Compd 2004;376:79.

[46] Krishna BV, Bose S, Bandyopadhyay A. J Biomed Mater Res B, Appl Biomater 2009;89B:481.

[47] Balla VK, Bose S, Bandyopadhyay A. Philos Mag 2010;90:3081.

[48] Kwok PJ, Oppenheimer SM, Dunand DC. Adv Eng Mater 2008;10:820.

[49] Jorgensen DJ, Dunand DC. Mater Sci Eng A 2010;527:849.

[50] Jorgensen DJ, Dunand DC. Acta Mater 2010;59:640.

[51] Neurohr AJ, Dunand DC. Acta Biomater 2011;7:1862.

[52] Raghavan V. J Phase Equil Diff 2010;31:186.

[53] Ye B, Matsen MR, Dunand DC. Acta Mater 2010;58:3851.

[54] Jackson CM, Wagner HJ, Wasilewski RJ. 55-Nitinol – the alloy with a memory: its physical metallurgy, properties, and applications, vol. 42. Washington, DC: National Aeronautics and Space Administration; 1972.

[55] Panico M, Brinson LC. Int J Solids Struct 2008;45:5613.

[56] Rajagopalan S, Little AL, Bourke MAM, Vaidyanathan R. Appl Phys Lett 2005;86:3.

[57] Tosun G, Ozler L, Kaya M, Orhan N. J Alloys Compd 2009;487:605.

[58] Bassani P, Giuliani P, Tuissi A, Zanotti C. J Mater Eng Perform 2009;18:594.

[59] Barrabés M, Sevilla P, Planell JA, Gil FJ. Mater Sci Eng C 2008;28:23.

[60] Huang H, Zhang H, Zhou L, Zheng HY. J Micromech Microeng 2003;13:693.

[61] Tane M, Ichitsubo T, Hyun SK, Nakajima H. J Mater Res 2005;20:135.

[62] Roy S, Butz B, Wanner A. Acta Mater 2010;58:2300.

[63] Ashby MF. The properties of foams and lattices. Royal society discussion meeting on engineered foams and porous materials. London: Royal Society; 2005. p. 15.

[64] Vaidyanathan R, Bourke MAM, Dunand DC. Acta Mater 1999;47:3353.

[65] Hu Q, Jin W, Liu XP, Cao MZ, Li SX. Mater Lett 2002;54:114.

[66] Strnadel B, Ohashi S, Ohtsuka H, Ishihara T, Miyazaki S. Mater Sci Eng A, Struct Mater, Prop Microstruct Process 1995;202:148.

[67] Duerig TW, Melton KN, Stoeckel D, Wayman CM. Engineering aspects of shape memory alloys. Oxford: Butterworth-Heinemann; 1990.

[68] Gibson LJ, Ashby MF. Cellular solids: structure and properties. Cambridge: Cambridge University Press; 1997.

[69] Clyne TW, Withers PJ. An introduction to metal matrix composites. New York, NY: Cambridge University Press; 1993.

[70] Brown LM, Clarke DR. Acta Metall 1975;23:821.

[71] Mortensen A. Concise encyclopedia of composite materials. Amsterdam, Netherlands: Elsevier; 2007.

[72] Shen H, Oppenheimer SM, Dunand DC, Brinson LC. Mech Mater 2006;38:933.